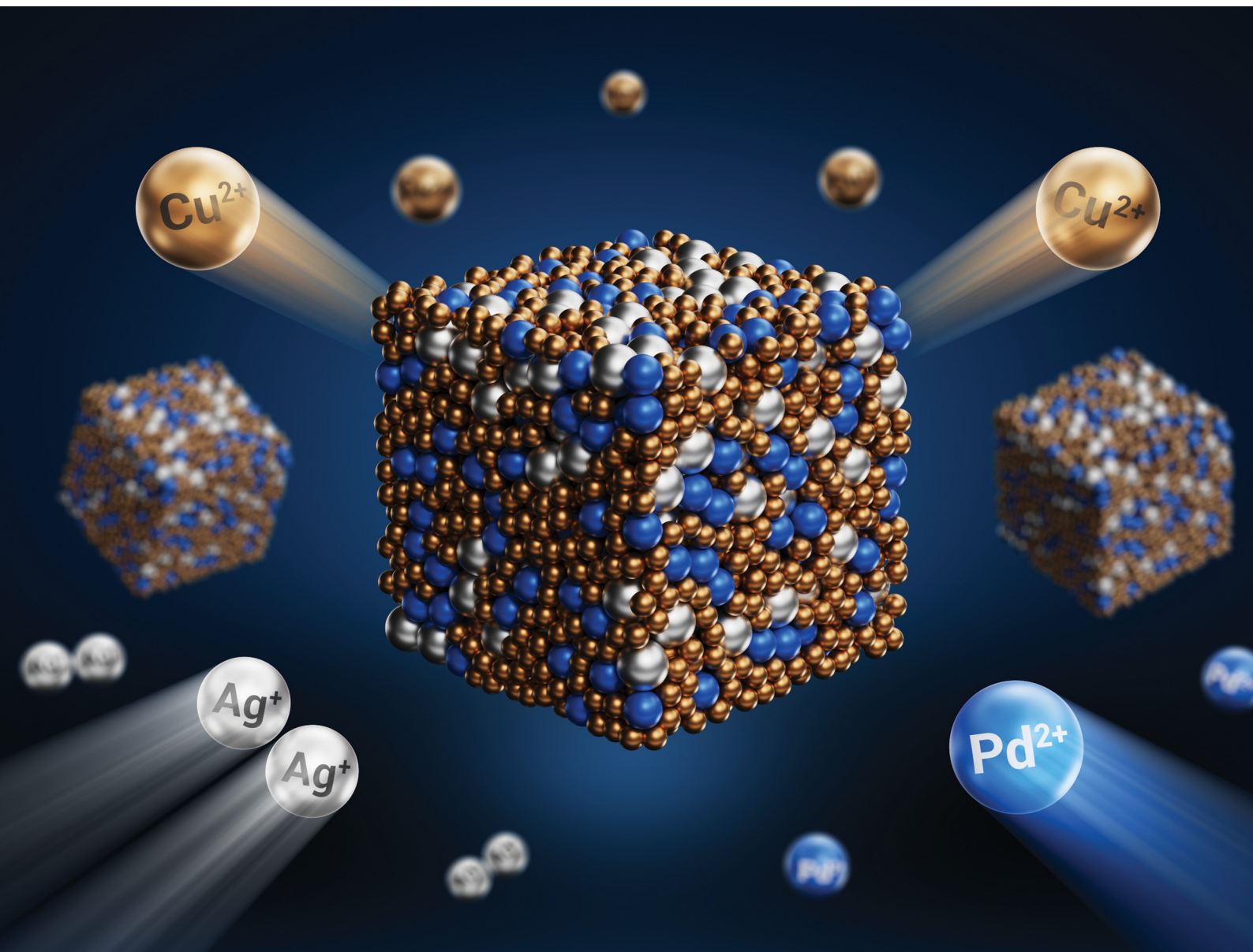


# ChemComm

Chemical Communications

rsc.li/chemcomm



ISSN 1359-7345

**COMMUNICATION**

Yaovi Holade *et al.*

Concerted galvanic replacement reactions towards  
trimetallic Cu-Ag-Pd nanostructures for glycerol  
electrocatalysis


 Cite this: *Chem. Commun.*, 2025, 61, 18798

 Received 5th September 2025,  
 Accepted 21st October 2025

DOI: 10.1039/d5cc05142h

[rsc.li/chemcomm](https://rsc.li/chemcomm)

# Concerted galvanic replacement reactions towards trimetallic Cu–Ag–Pd nanostructures for glycerol electrocatalysis

 Eddy Zakharia,<sup>a</sup> Zahra Hagheh Kavousi,<sup>ib</sup> Bonito Aristide Karamoko,<sup>ib</sup> Erwan Oliviero,<sup>ib</sup> Valerie Bonniol,<sup>ib</sup> Eddy Petit,<sup>b</sup> Valerie Flaud,<sup>bc</sup> David Cornu,<sup>ib</sup> Mikhael Bechelany,<sup>ib</sup> and Yaovi Holade<sup>ib</sup>\*<sup>ad</sup>

**We report a proof-of-concept synthesis of Cu–Ag–Pd nanostructures via concerted galvanic replacement reactions between copper(0) and silver(i)–palladium(ii). This methodology enables dramatic enhancement of the electrocatalytic properties of the derived materials by adjusting the lattice strain depending on the amounts of incoming Pd and Ag, and outgoing Cu from the template.**

Over the past decade, several methods for synthesising multi-metallic nanostructures have emerged to elegantly combine electronic, ligand and synergistic effects in order to adjust structure–activity relationships in several fields such as catalysis, biology and sensing.<sup>1–3</sup> For trimetallic nanomaterials based on noble metals, conventional synthesis by low-energy co-deposition (chemical reduction, electrodeposition, *etc.*) does not allow specific defects or porosity to be created directly in order to manipulate the catalytic properties.<sup>3,4</sup> In this context, the galvanic replacement reaction (GRR) is of interest as it enables the controlled replacement of the atoms of one metal with those of a more noble metal (*i.e.* one with a higher oxidation potential than the initial template metal).<sup>5,6</sup> The GRR principle has enabled the synthesis of various bimetallics.<sup>5–7</sup> The extension to at least three metals would be promising for medium- to high-entropy materials, where nanoalloying, nanoporosity, and strain could coexist, depending on the size of the metals entering or leaving the initial architecture.

Targeting Pd–Cu–M (M = Au, Pt) systems, Sara E. Skrabalak and colleagues investigated GRR between PdCu intermetallic nanoparticles and Au(III) or Pt(IV) ionic species and found that the synthesis produces exotic trimetallic architectures, ranging from core–shell to Janus particles, due to the simultaneous

effects of Ostwald and Kirkendall maturation.<sup>3,4</sup> This suggests a challenge of forming an alloy phase due to segregation energy,<sup>8</sup> particularly given that the initial state comprises two different metals. Among noble metals, Cu has the lowest standard redox potential  $E^\circ(\text{Cu}^{2+}/\text{Cu}) = 0.34$  V vs. standard hydrogen electrode (SHE). So, this offers many possibilities of performing GRR of Cu by M (M = Ag, Pd, Pt, Au, *etc.*). Hence, the lattice mismatch between Cu and M is expected to cause strain effects that modify the d-band centre and regulate the binding energy between the active sites and the reactants and intermediates, consequently improving the catalytic activity.<sup>1,9,10</sup> For example, it was reported that the partial GRR of Cu by Ag produces an Ag–Cu bimetal catalyst with improved activity for the oxygen reduction reaction (ORR) in an alkaline electrolyte.<sup>9</sup>

Given the inconclusive results of previous tests on the formation of trimetallic alloys by GRR from a preformed bimetallic,<sup>3,4</sup> one question remains unanswered: would it be possible to obtain  $\text{Cu}_{1-x-y}\text{Ag}_x\text{Pd}_y$  materials ( $x$  and  $y$  are the atomic fractions of Ag and Pd) by GRR from Cu? This would allow the intrinsic properties of Cu, Ag and Pd to coexist within the same material. While GRR of Ag by Au ( $3\text{Ag} + \text{Au(III)} \rightarrow 3\text{Ag(I)} + \text{Au}$ ) involves removing more atoms and adding fewer to almost the same fcc crystallographic system,<sup>5,7,11</sup> the GRR of Cu by Ag ( $\text{Cu} + 2\text{Ag(I)} \rightarrow \text{Cu(II)} + 2\text{Ag}$ ) is captivating because the Ag lattice parameter (face-centred cubic, fcc) is much larger than that of Cu fcc. The same observation can be made in the case of GRR of Cu by Pd ( $\text{Cu} + \text{Pd(II)} \rightarrow \text{Cu(II)} + \text{Pd}$ ), since the fcc lattice parameter of Pd is larger than that of Cu. Arguably, the simultaneous GRR by both Pd and Ag should enable adjustment of electrocatalytic performance by regulating surface stress effects, provided that the appropriate synthesis conditions are found.

To address these challenges, we conducted a study on proof-of-concept concerted galvanic replacement reactions involving Cu, Ag and Pd. We used a carbon-supported copper nanoparticle model (7 wt% Cu/C) to target low-loading carbon-supported Cu–Ag–Pd trimetallic nanostructures (7–9 wt%  $\text{Cu}_{1-x-y}\text{Ag}_x\text{Pd}_y/\text{C}$ ). We evaluated the catalytic properties with respect to the glycerol

<sup>a</sup> Institut Européen des Membranes, IEM, UMR 5635, Univ Montpellier, ENSCM, CNRS, 34090, Montpellier, France. E-mail: yaovi.holade@enscm.fr

<sup>b</sup> Institut Charles Gerhardt, ICGM, UMR 5253, Univ Montpellier, ENSCM, CNRS, 34090, Montpellier, France

<sup>c</sup> PAC Chimie Balard, Univ Montpellier, CNRS, ENSCM, 34090, Montpellier, France

<sup>d</sup> Institut Universitaire de France (IUF), 75005, Paris, France



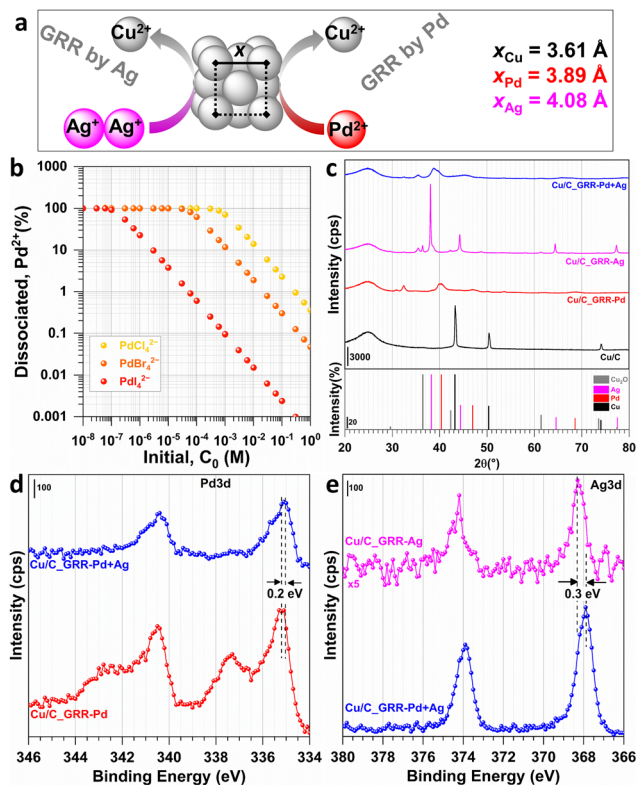


Fig. 1 (a) Scheme of the concerted GRR towards trimetallic nanoparticles CuAgPd. (b) Percent of Pd<sup>2+</sup> for different initial concentrations of palladium(II) precursors. (c) XRD patterns. (d) High-resolution XPS of Pd 3d. (e) High-resolution XPS of Ag 3d.

electrooxidation reaction to validate the hypothesis of enhanced catalytic efficiency. The ultimate goal is to reduce the amount of precious metals in electrocatalysts to promote low-energy biomass conversion in green hydrogen electrolyzers.<sup>12,13</sup>

Our investigation model initially involves synthesizing Cu/C and then performing GRR simultaneously in the presence of Pd(II) and Ag(I) precursors. This results in the formation of the target materials, Cu<sub>1-x-y</sub>Ag<sub>x</sub>Pd<sub>y</sub>/C, with lattice parameter expansion. This expansion leads to a change in the metal-metal bond distance and modulation of the electrocatalytic activity. Fig. 1a illustrates the designed methodology. The difference in lattice parameters between Cu and Pd suggests that GRR of Cu by Pd ( $\text{Cu} + \text{Pd}^{2+} \rightarrow \text{Cu}^{2+} + \text{Pd}$ ,  $K_{\text{eq},1} = 2.1 \times 10^{19}$ ) is accompanied by a tensile strain (rather than compressive strain)<sup>1,10</sup> of 7.8% relative to pristine Cu during the formation of Cu-Pd. Besides, the GRR of Cu by Ag ( $\text{Cu} + 2\text{Ag}^+ \rightarrow \text{Cu}^{2+} + 2\text{Ag}$ ,  $K_{\text{eq},2} = 3.9 \times 10^{15}$ ) is accompanied by tensile strain of 13.0% relative to pristine Cu. Indeed, the three metals crystallize in the fcc system with the lattice parameters of 3.61 Å (Cu), 3.89 Å (Pd) and 4.08 Å (Ag). Also, the trend in standard redox potentials is  $E^\circ = 0.34$ , 0.91 and 0.80 V vs. SHE for Cu<sup>2+</sup>/Cu, Pd<sup>2+</sup>/Pd and Ag<sup>+</sup>/Ag, respectively. Therefore, in the ideal scenario, the simultaneous GRR of Cu by Pd and by Ag ( $2\text{Cu} + \text{Pd}^{2+} + 2\text{Ag}^+ \rightarrow 3\text{Cu}^{2+} + \text{Pd} + 2\text{Ag}$ ) should produce a tensile strain in the range of 7.8–13.0% relative to the pristine Cu depending on the amount of incoming Pd and Ag and outgoing Cu. This is a tool for tuning catalytic performance.<sup>1,10</sup>

Given that the commonly used water-soluble Pd(II) precursor is K<sub>2</sub>PdCl<sub>4</sub>, we first determined the nature of the Pd(II) species (*i.e.* PdCl<sub>4</sub><sup>2-</sup> or Pd<sup>2+</sup>) in the GRR media by examining the impact of the initial K<sub>2</sub>PdCl<sub>4</sub> concentration on the proportion of Pd<sup>2+</sup> ions in water. This data is crucial for comprehending the GRR's driving force, as the complexation of metal cations decreases the redox potentials. Here, the values are  $E^\circ = 0.91$ , 0.62, 0.49 and 0.18 V vs. SHE for Pd<sup>2+</sup>/Pd, PdCl<sub>4</sub><sup>2-</sup>/Pd, PdBr<sub>4</sub><sup>2-</sup>/Pd, and PdI<sub>4</sub><sup>2-</sup>/Pd, respectively. Consequently, the GRR's driving force between Cu(0) and Pd(II) decreases significantly when Pd<sup>2+</sup> complexes with halide ions. Therefore, no GRR should occur between Cu(0) and PdI<sub>4</sub><sup>2-</sup>, as the Nernst potential of PdI<sub>4</sub><sup>2-</sup>/Pd is likely to be lower than that of Cu<sup>2+</sup>/Cu. However, GRR could occur between Pd<sup>2+</sup> and Ag(0) from GRR-Ag. Fig. 1b shows Pd<sup>2+</sup> amounts for various initial concentrations of Pd(II) precursors. In our GRR conditions, the initial concentration of K<sub>2</sub>PdCl<sub>4</sub> is 2.9 mM (see SI). So, according to Fig. 1b, 71% of the introduced PdCl<sub>4</sub><sup>2-</sup> is in the form of Pd<sup>2+</sup>, which should be sufficient to react with Cu(0) since a partial GRR of Cu by Pd was targeted. Furthermore, as about 30% of the Pd(II) is present as a PdCl<sub>4</sub><sup>2-</sup>, the mixture is initially yellow due to ligand-to-metal charge transfer phenomena.<sup>14,15</sup> Therefore, since the nanoparticles were collected by centrifugation after GRR, when the supernatant is colourless, this indicates successful replacement. Herein, the Cu/C starting material was synthesised using an impregnation and calcination approach.<sup>16</sup> The X-ray diffraction (XRD) results in Fig. S1 (SI) demonstrate that a calcination at 600 °C in a nitrogen atmosphere is sufficient to trigger the formation of metallic copper.

Bulk quantitative analysis by inductively coupled plasma optical emission spectrometry (ICP-OES; Table S1, SI) yielded a metal content of  $(6.9 \pm 0.7)$  wt%, consistent with the targeted 7–10 wt%. Interestingly, the mass variation after GRR was found to be 26%, 7% and 15% for GRR-Pd, GRR-Ag, and GRR-Ag + Pd, respectively. These results reinforce the hypothesis that GRR occurred because replacing Cu with a heavier metal (1 : 2 atomic ratio in the case of Ag, and 1 : 1 in the case of Pd) increases the mass. The difference between the experimental and theoretical values for GRR-Ag and GRR-Ag + Pd can be explained by slower reaction kinetics between Cu(0) and Ag(I). According to ICP-OES analysis, stopping the GRR deliberately after the same reaction time while targeting a maximum of 50% Cu replacement leads to the following atomic compositions: Cu<sub>60</sub>Pd<sub>40</sub>, Cu<sub>82</sub>Ag<sub>18</sub> and Cu<sub>63</sub>Pd<sub>21</sub>Ag<sub>16</sub> (Table S1, SI). Fig. 1c confirms the crystallinity of Cu/C, which has an fcc structure with diffraction peaks at 43.4°, 50.5° and 74.2° for the Cu(111), Cu(200) and Cu(220) planes, respectively (Table S2, SI). After GRR, the disappearance of the Cu peaks and the apparition of new peaks, is indicative of the successful formation of a new Cu<sub>1-x-y</sub>Ag<sub>x</sub>Pd<sub>y</sub>/C phase (plus oxides by-products), with a significant variation in the peak intensities and interplanar spacing (Table S3, SI). The experimental values of lattice strain of 13.0%, 6.6% and 9.5% for GRR-Pd, GRR-Ag, and GRR-Ag + Pd, respectively, confirm the hypothesis of lattice mismatch during GRR. The specific surface area ranges from 180 to 230 m<sup>2</sup> g<sup>-1</sup> (Table S3 and Fig. S2, SI), which is similar to that of Vulcan carbon-supported nanocatalysts.<sup>17</sup>



We then sought to characterise the surface state using X-ray photoelectron spectroscopy (XPS). High-resolution XPS spectra of Pd 3d (Fig. 1d), Ag 3d (Fig. 1e) and Cu 2p (Fig. S3, SI) confirm the presence of the three metal species (Tables S4 and S5, SI). As with XRD, Fig. 1d confirms the presence of PdO for GRR-Pd with binding energies at 336.8 and 342.3 eV,<sup>18</sup> which is currently inexplicable, even though GRR was performed at a neutral pH where metal hydroxides would be expected to be found based on the Pd(II)-chloride speciation diagrams.<sup>14,15</sup> Furthermore, the surface atomic composition (Table S5, SI) is consistent with bulk analysis by ICP-OES, thus validating the homogeneity of the materials. The downshift in the binding energies of the Pd 3d and Ag 3d peaks (Fig. 1d and e) and the upshift in the Cu 2p peak (Table S5, SI) endorse the change in metal-metal distance revealed by XRD (Table S3, SI). This indicates electronic exchange between the different metals within  $\text{Cu}_{1-x-y}\text{Ag}_x\text{Pd}_y/\text{C}$ .<sup>1</sup>

To further support the creation of  $\text{Cu}_{1-x-y}\text{Ag}_x\text{Pd}_y$  nanostructures, we performed scanning transmission electron microscopy (STEM) studies. Line scanning analysis of Fig. 2a-d and Fig. S4, S5 (SI) shows the atomic-scale coexistence of Cu, and Pd and/or Ag. This confirms our initial hypothesis of homogenous phase and rules out phase segregation in the trimetallic system,<sup>3,4</sup> despite the different kinetics of the two redox pairs involved (Pd(II)/Pd and Ag(I)/Ag) when reacting with Cu. Fig. 3a-c show the atomic-scale analysis for GRR-Ag + Pd. Extended TEM, HRTEM and intensity profile studies, as reported in Fig. S6-S14 (SI), for mono-, bi- and tri-metallic structures, highlight the synthesis of 20–50 nm nanoparticles, which are mainly enclosed by the (111) crystallographic plane, as the interplanar

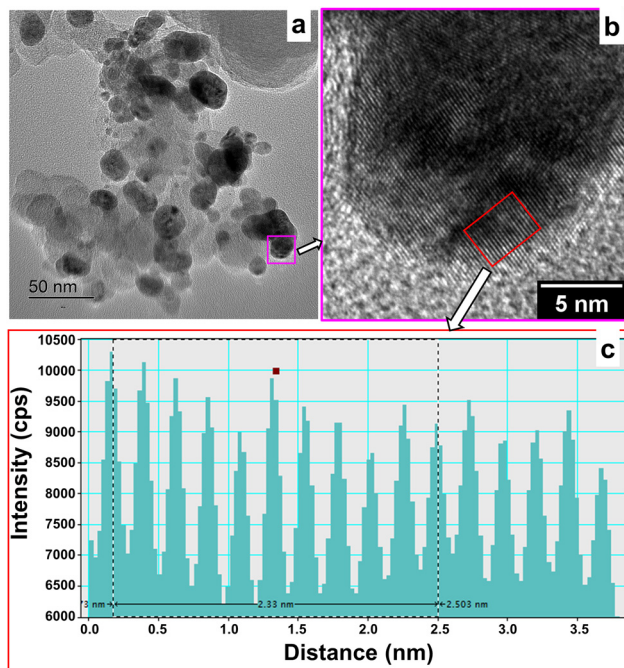


Fig. 3 (a) Bright-field TEM image, (b) HRTEM image, and (c) intensity profiles extracted from (b) for Cu/C\_GRR-Ag + Pd.

spacing is 0.20–0.24 nm. Importantly, post-mortem TEM analysis (Fig. S15 and S16, SI) of GRR-Ag + Pd after accelerated glycerol electro-oxidation supports the integrity of the nanoparticles.

We next used voltammetry in alkaline media to validate the GRR realization and then interrogate the electrocatalytic activity of the resulting materials, as the three metals involved (Cu, Pd, Ag) have different electrochemical signatures.<sup>19–22</sup> The results are presented in Fig. 4a–d and Fig. S17–S25 (SI). To ensure a fair comparison, we used the benchmark Pd/C. In Fig. 4a, waves A1 and A2 are associated with metal-to-hydroxide and hydroxide-to-oxide processes. Peak C1 is attributed to the reduction of PdO to Pd,<sup>19–21</sup> occurring at potentials of 0.59, 0.60 and 0.61 V *versus* the reversible hydrogen electrode (RHE) for Pd/C, Cu/C\_GRR-Pd and Cu/C\_GRR-Pd + Ag, respectively. According to Rand and Woods' theory, the slight upshift is characteristic of alloy phase formation.<sup>23</sup> The C2 peak at 1.0 V *vs.* RHE is ascribed to  $\text{Ag}_2\text{O}$ -to-Ag reduction.<sup>19–21</sup> Although post-mortem STEM-EDX confirmed the presence of silver within Cu/C\_GRR-Pd + Ag, the absence of this redox peak is consistent with the literature on PdAg/C materials when the silver atomic composition is 50% or less, which has been attributed to surface reorganization.<sup>19–21</sup>

Fig. S17 and S18 (SI) confirm that both Cu and Ag do have significant activity towards glycerol oxidation at potentials below 1.2 V *vs.* RHE. The comparative Table S6 (SI) shows that the developed low-loading  $\text{Cu}_{1-x-y}\text{Ag}_x\text{Pd}_y/\text{C}$  nanostructures (7–9 wt%, 15–31  $\mu\text{g}_{\text{Pd}} \text{cm}^{-2}$ ) outperformed some relevant metallic electrocatalysts. Taking into account both the geometric surface and the mass of the active metal (Pd), Fig. 4b confirms the enhanced activity for GRR-derived nanostructures. Based on the

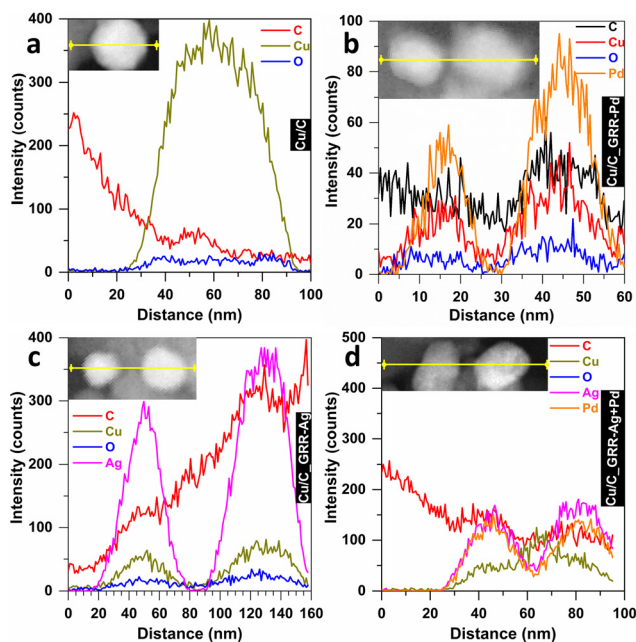
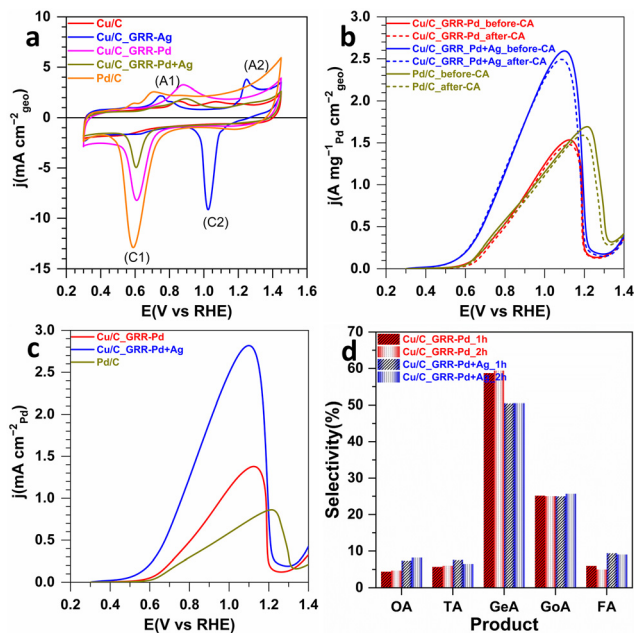


Fig. 2 EDX line-scan intensity profiles and inset images of the corresponding high-angle annular dark-field STEM images: (a) before GRR, and (b)–(d) after GRR. (a) Cu/C, (b) Cu/C\_GRR-Pd, (c) Cu/C\_GRR-Ag, and (d) Cu/C\_GRR-Pd + Ag.





**Fig. 4** (a) CV in 1 M KOH ( $50 \text{ mV s}^{-1}$ ,  $25^\circ\text{C}$ ). (b) Forward scan in 1 M KOH + 1 M glycerol ( $5 \text{ mV s}^{-1}$ ,  $25^\circ\text{C}$ ), current density by the mass of active metal (Pd) and the geometric surface area. (c) Forward scan in 1 M KOH + 1 M glycerol ( $5 \text{ mV s}^{-1}$ ,  $25^\circ\text{C}$ ), current density by ECSA of the active metal (Pd). (d) Product distribution from HPLC analysis upon acid neutralization after bulk electrolysis (OA: oxalic acid; TA: tartaric acid; GeA: glyceric acid; GoA: glycolic acid; FA: formic acid).

electrochemically active surface area of palladium, the peak current density (Fig. 4c) is  $2.8$ ,  $1.4$ , and  $0.8 \text{ mA cm}_{\text{Pd}}^{-2}$ , for Cu/C\_GRR-Pd + Ag, Cu/C\_GRR-Pd and Pd/C-commercial, respectively. The electrochemical impedance spectroscopy results of Fig. S23 (SI) show that the improvement of the catalytic activity results from the reduced charge transfer resistance during the glycerol oxidation. These findings confirm the initially hypothesized possibility of enhancing the catalytic performance by the concerted GRR. We finally performed bulk glycerol electrolysis (Fig. S25–S27, SI) to interrogate any discrepancy in the reaction products. The quantitative data of Table S7 (SI) highlight a high faradaic efficiency of 85–100%. Fig. 4d shows that the trimetallic electrocatalyst improves slightly the selectivity towards oxalic and formic acids in addition to the high specific activity and durability (Fig. S22, S25–S27, SI). However, Fig. S28 (SI) highlights a loss of Cu.

In summary, we have proven the feasibility of concerted galvanic replacement reactions between Cu(0), Ag(I) and Pd(II), with the target of creating a lattice mismatch between native Cu and the new structure. Electrocatalytic tests demonstrate that precious metals (Pd) can be significantly reduced in favour of more abundant metals (Cu, Ag) while maintaining selectivity and amplifying activity. Specifically, the new synthesis approach enables the catalytic performance of the glycerol oxidation reaction to be adjusted to achieve a faradaic efficiency of 85–100% by controlling the tensile strain within the range of 7.8–13.0%, relative to pristine Cu, depending on the amount of Pd and Ag input. These results open up new prospects for accessing advanced functional multi-metal nanostructures.

This work was funded by the French National Research Agency (ANR-22-CE43-0004), the I-SITE Excellence Program of the University of Montpellier under the Investissements France 2030 (project NANOGATE), and Institut Universitaire de France (IUF). SEM and TEM analyses were carried out at ‘PAC Chimie Balard’, analytical facilities of Univ Montpellier, CNRS, ENSCM.

## Conflicts of interest

There are no conflicts to declare.

## Data availability

The data supporting the findings of this study are available within the article and its supplementary information (SI). Supplementary information: experimental details; extended characterization. See DOI: <https://doi.org/10.1039/d5cc05142h>.

## Notes and references

- Z.-Y. Chen, L.-T. Li, F.-M. Zhao, Y.-H. Zhu and Y.-Q. Chu, *ChemElectroChem*, 2024, **11**, e202400154.
- Y. Chen, A. Zohaib, H. Sun and S. Sun, *Chem. Commun.*, 2025, **61**, 12097–12114.
- N. Kar, M. McCoy, X. Zhan, J. Wolfe, Z. Wang and S. E. Skrabalak, *Nanoscale*, 2023, **15**, 3749–3756.
- A. N. Chen, E. J. Endres, H. M. Ashberry, S. L. A. Bueno, Y. Chen and S. E. Skrabalak, *Nanoscale*, 2021, **13**, 2618–2625.
- A. G. M. da Silva, T. S. Rodrigues, S. J. Haigh and P. H. C. Camargo, *Chem. Commun.*, 2017, **53**, 7135–7148.
- A. N. Chen, S. M. McClain, S. D. House, J. C. Yang and S. E. Skrabalak, *Chem. Mater.*, 2019, **31**, 1344–1351.
- H. Cheng, C. Wang, D. Qin and Y. Xia, *Acc. Chem. Res.*, 2023, **56**, 900–909.
- G. A. Kamat, C. Yan, W. T. Osowiecki, I. A. Moreno-Hernandez, M. Ledendecker and A. P. Alivisatos, *J. Phys. Chem. Lett.*, 2020, **11**, 5318–5323.
- R. Thota, S. Sundari, S. Berchmans and V. Ganesh, *ChemistrySelect*, 2017, **2**, 2114–2122.
- P. Strasser, S. Koh, T. Anniyev, J. Greeley, K. More, C. Yu, Z. Liu, S. Kaya, D. Nordlund, H. Ogasawara, M. F. Toney and A. Nilsson, *Nat. Chem.*, 2010, **2**, 454–460.
- J. Xu, Q. Yun, H. Zhang, Y. Guo, S. Ke, J. Wang, X. Zhu and C. Kan, *Chem. Commun.*, 2021, **57**, 8332–8335.
- M. Braun, C. S. Santana, A. C. Garcia and C. Andronescu, *Curr. Opin. Green Sustainable Chem.*, 2023, **41**, 100829.
- Y. Holade, T. W. Napporn and K. B. Kokoh, *Curr. Opin. Electrochim.*, 2025, **49**, 101625.
- J.-F. Boily and T. M. Seward, *Geochim. Cosmochim. Acta*, 2005, **69**, 3773–3789.
- C. Drew Tait, D. R. Janecky and P. S. Z. Rogers, *Geochim. Cosmochim. Acta*, 1991, **55**, 1253–1264.
- R. Fan, C. Chen, M. Han, W. Gong, H. Zhang, Y. Zhang, H. Zhao and G. Wang, *Small*, 2018, **14**, 1801953.
- Y. Holade, C. Morais, K. Servat, T. W. Napporn and K. B. Kokoh, *Phys. Chem. Chem. Phys.*, 2014, **16**, 25609–25620.
- Y. Holade, C. Canaff, S. Poulin, T. W. Napporn, K. Servat and K. B. Kokoh, *RSC Adv.*, 2016, **6**, 12627–12637.
- Y. Holade, C. Morais, K. Servat, T. W. Napporn and K. B. Kokoh, *ACS Catal.*, 2013, **3**, 2403–2411.
- S. T. Nguyen, H. M. Law, H. T. Nguyen, N. Kristian, S. Wang, S. H. Chan and X. Wang, *Appl. Catal., B*, 2009, **91**, 507–515.
- G. Li, L. Jiang, Q. Jiang, S. Wang and G. Sun, *Electrochim. Acta*, 2011, **56**, 7703–7711.
- N. E. Şahin, C. Comminges, S. Arrii, T. W. Napporn and K. B. Kokoh, *ChemElectroChem*, 2021, **8**, 1362–1368.
- D. A. J. Rand and R. Woods, *J. Electroanal. Chem. Interfacial Electrochem.*, 1972, **36**, 57–69.

